The Astrophysical Journal Letters, 934:L11 (9pp), 2022 July 20 https://doi.org/10.3847/2041-8213/ac7f44

Kinematic Evidence for an Embedded Planet in the IM Lupi Disk

Harrison J. Verrios[1], Daniel J. Price[1], Christophe Pinte[1,2], Thomas Hilder[1], and Josh Calcino[3]
[1] School of Physics and Astronomy, Monash University, Clayton, Vic 3800, Australia; daniel.price@monash.edu
[2] Université Grenoble Alpes, CNRS, IPAG, F-38000 Grenoble, France
[3] Theoretical Division, Los Alamos National Laboratory, Los Alamos, NM 87545, USA
Received 2022 March 28; revised 2022 June 27; accepted 2022 June 30; published 2022 July 22

Abstract

We test the hypothesis that an embedded giant planet in the IM Lupi protostellar disk can produce velocity kinks seen in CO line observations as well as the spiral arms seen in scattered light and continuum emission. We inject planets into 3D hydrodynamics simulations of IM Lupi, generating synthetic observations using Monte Carlo radiative transfer. We find that an embedded planet of 2–3 $M_{\rm Jup}$ can reproduce non-Keplerian velocity perturbations, or "kinks", in the ^{12}CO $J = 2$–1 channel maps. Such a planet can also explain the spiral arms seen in 1.25 mm dust continuum emission and 1.6 μm scattered-light images. We show that the wake of the planet can be traced in the observed peak velocity map, which appears to closely follow the morphology expected from our simulations and from analytic models of planet–disk interaction.

Unified Astronomy Thesaurus concepts: Exoplanet formation (492); Exoplanet migration (2205); Protoplanetary disks (1300); Planet formation (1241); Circumstellar disks (235); Hydrodynamical simulations (767); Planetary-disk interactions (2204)

1. Introduction

IM Lupi, a young star located 155.8 ± 0.5 pc away (Lindegren et al. 2018), hosts a large and spectacular protoplanetary disk (Panić et al. 2009; Cleeves et al. 2016; Avenhaus et al. 2018; Pinte et al. 2018a). Observations in the ^{12}CO $J = 2$–1 spectral line from the Disk Substructures at High Angular Resolution Project (DSHARP; Huang et al. 2018; Andrews et al. 2018) showed localized deviations from Keplerian velocity in multiple velocity channels. More recently, the Molecules with ALMA at Planet-forming Scales Survey (MAPS; Oberg et al. 2021) has confirmed these structures are present within the disk and are not observational artifacts. Pinte et al. (2020) predicted that a massive planet located at 117 au from the host star could be the cause of these deviations, referred to as *kinks* (see the definition in Calcino et al. 2022). Detecting this planet using traditional observational methods, such as radial velocities, transits, or direct imaging, is currently impossible as its orbit is too large and the planet is hidden within an optically thick disk of gas and dust (e.g., Pinte et al. 2018a).

Scattered-light images of IM Lupi (Avenhaus et al. 2018) provide further evidence for embedded planets. This spectacular image revealed spiral structures in the upper layer of the disk traced by scattered light from submicron grains. Additionally, observations from DSHARP in the 1.25 mm dust continuum show spiral arms and gaps in the midplane dust disk (Andrews et al. 2018).

IM Lupi is important because it is one of only a few disks that show large-scale spiral arms in millimeter-continuum emission. The other well-studied example is Elias 2–27 where there are two main hypotheses (Meru et al. 2017): an embedded planet (Meru et al. 2017) or gravitational instability (Forgan et al. 2018; Hall et al. 2018; Paneque-Carreño et al. 2021; Veronesi et al. 2021). The main prediction has been that gravitational instability will produce flocculent spiral structure and hence "kinks everywhere" (Hall et al. 2020), whereas planets should produce more localized deviations from Keplerian motion (Pinte et al. 2020). Gravitational instability also requires a massive disk, while embedded planets do not require this.

Our aim in this Letter is to investigate whether an embedded planet in the disk can explain the observed substructures in IM Lupi. We model disks using hydrodynamical simulations, creating synthetic observations using Monte Carlo radiative transfer. Comparing our models to observations enables us to constrain the mass and location of the planet. We also predict kinematic perturbations from the planet wake in the peak velocity map, which we confirm are present in the observational data. Our Letter is organized as follows: we describe our methods and initial conditions in Section 2, present our findings in Section 3, discuss the implications and limitations in Section 4, and conclude in Section 5.

2. Methods

2.1. Initial Conditions

We performed smoothed particle hydrodynamics (SPH) simulations of planet–disk interaction using PHANTOM (Price et al. 2018). We modeled the disk with 10^7 SPH particles, set up initially to follow a tapered power-law surface density profile given by

$$\Sigma = \Sigma_c \left(\frac{R}{R_c}\right)^{-p} \exp\left[-\left(\frac{R}{R_c}\right)^{2-p}\right]. \quad (1)$$

We assumed $p = 0.48$ (Pinte et al. 2018a). We used $R_c = 150$ au instead of the Pinte et al. (2018a) value of $R_c = 284$ au for computational convenience. We assumed a vertically isothermal equation of state $P = c_s^2(R)\rho$ with $c_s \propto R^{-q}$, $q = 0.31$, and the sound speed normalized to give an aspect ratio $H/R = 0.129$ at a radius of 100 au (Cleeves et al. 2016; Pinte et al. 2018a). We adopted a stellar mass of 1.12 $M_\odot$ (Andrews et al. 2018) with the star modeled as a sink particle with an

accretion radius of 1 au. We set up the disk initially between $r_{\rm in} = 30$ au and $r_{\rm out} = 970$ au (Panić et al. 2009), as we were not concerned with the inner disk structure. The vertically averaged ratio of smoothing length to disk scale height, $\langle h \rangle / H$, varies between $\approx 1/20$ at 200 au and $1/5$ at 30 au, with around 10 resolution lengths per scale height at the final planet location and ≈ 5 at the height of the CO and scattered-light emitting layer in IM Lupi (Law et al. 2021). We adopted a total gas mass of $0.1\,M_{\odot}$, as determined by Cleeves et al. (2016). We also performed simulations with a disk mass of $0.01\,M_{\odot}$, but found that the higher disk mass better reproduces the scattered-light image because the submicron-sized grains remain well coupled in the top layers of the disk.

We included dust in the simulations using the MULTIGRAIN one-fluid algorithm (Price & Laibe 2015; Ballabio et al. 2018; Hutchison et al. 2018; Price et al. 2018). We modeled 11 grain sizes spanning $a_{\rm min} = 1.0\,\mu$m to $a_{\rm max} = 2300\,\mu$m on a logarithmically spaced grid with a power-law distribution with a slope of -3.5. We assumed a gas-to-dust ratio of 57 in order to give a total dust mass of $1.7 \times 10^{-3}\,M_{\odot}$, as determined by Pinte et al. (2018a).

2.2. Embedded Planets

Pinte et al. (2020) predicted a planet orbiting IM Lupi with a semimajor axis of 117 au, based on the location of the velocity kink in the ^{12}CO channel in the DSHARP data. Since our planets migrate over the course of the simulation, we placed the planet initially at 150 au, which results in a planet at approximately the correct radius. The initial fast migration (10 au kyr^{-1}) occurs mainly because it takes several orbits for the planet to open a gap. After this the migration steadies to ≈ 2.3 au kyr^{-1}.

A consequence of the relatively high disk mass is that our planets, if modeled as "vacuum cleaner" sink particles, would accrete a large amount of mass (up to 10 times their initial mass in the first 50 orbits). Since this is largely an artifact of the boundary condition employed (Ayliffe & Bate 2010), we instead modeled our planet as a nonaccreting sink particle with a softened gravitational potential, similar to the procedure in Szulágyi et al. (2016). We assumed a cubic B-spline softening kernel (Price & Monaghan 2007) that becomes Keplerian at a radius $2h_{\rm soft}$, where $h_{\rm soft}$ is the softening length (see, e.g., Price et al. 2018). This allows the sink particle mass for the planet to remain constant throughout the simulation, while producing the correct interactions with the surrounding gas and dust. We use a constant softening length of $h_{\rm soft} = 1.75$ au for the planet. To model the effects that the mass of the planet has on the disk, we performed four simulations, each with a single planet of mass 2, 3, 5, and 7 Jupiter-masses, respectively, plus one simulation with no planet. We kept all other initial conditions the same between each simulation.

2.3. Radiative Transfer

We postprocessed our 3D simulations using MCFOST (Pinte et al. 2006, 2009). We assumed the IM Lupi disk to be located 156 pc from the observer (Klioner et al. 2018) with 230° inclination (i.e., 50° but rotating clockwise) and a position angle of 53° (Avenhaus et al. 2018). We assumed $T_{\rm eff} = 3900$ K and $R_{*} = 2.15\,R_{\odot}$ (Pinte et al. 2018a) for the central star.

We produced channel maps with a channel spacing of 0.05 km s^{-1}, from -2.4 to $+2.4$ km s^{-1}. For the channel maps we assumed turbulent broadening of $v_{\rm turb} = 0.08$ km s^{-1} and $f_{\rm UV} = 0.09$ (Pinte et al. 2018a). We adjusted the azimuthal location of the planet based on Pinte et al. (2020), giving an azimuthal angle of 30° (clockwise from north). To avoid CO being too bright in the outer disk we adopted a slightly lower (fixed) ^{12}CO-to-H$_2$ ratio of 1×10^{-5} compared to 5×10^{-5} assumed previously (Pinte et al. 2018a). This is likely due to our reduced value of $R_{\rm c}$.

We assumed a wavelength of 1.25 mm to produce the dust continuum image (Huang et al. 2018) and a wavelength of 1.6 μm to produce the scattered-light image (Avenhaus et al. 2018). For the scattered-light comparison, we computed the polarized intensity (PI) image by combining the Q and U Stokes parameters (Pinte et al. 2006). We assumed spherical grains (Mie scattering) to compute the polarized emission, as described in Pinte et al. (2006), assuming silicate grains (Weingartner & Draine 2001) with grain sizes and distributions taken from the hydrodynamic model. To match both the continuum and scattered-light images, we needed to rescale the grain sizes as in Pinte et al. (2019), scaling the notional Stokes numbers from the hydrodynamical simulations (down) by a factor of 10. This mainly suggests that grains are not spherical (see Section 4).

3. Results

3.1. Kinks and Non-Keplerian Features in Channel Maps

Figure 1 shows the observed ^{12}CO $J = 2$–1 channel maps of the IM Lupi disk from the MAPS project (Oberg et al. 2021). A typical Keplerian butterfly pattern is visible. Distinct CO-emitting surfaces from the top and bottom of the disk are also evident (see Pinte et al. 2018a). On top of this butterfly pattern we indicate (with arrows) at 16 locations where "kinks" or other perturbations away from Keplerian motion are visible in the data. This seemingly argues against a planetary origin since previous papers suggested that an embedded planet should produce only localized velocity perturbations (Pinte et al. 2018b, 2020).

Figure 2 shows the synthetic channels from our simulation with a $3M_{\rm J}$ planet. In all locations where a non-Keplerian signature was indicated in the data (arrows), we find a counterpart in the model that is significant in residuals from a no-planet model (see the Appendix). Essentially a kink occurs every time the planet wake crosses the channel, as predicted analytically by Bollati et al. (2021). The close match between the predicted and actual kinematic signatures in the channel maps, while not proof, shows that the hypothesis of a single embedded planet can explain the widespread non-Keplerian signatures in the disk without recourse to large-scale instabilities.

3.2. Spiral Arms in Scattered Light

Figure 3 compares the VLT/SPHERE image of IM Lupi from Avenhaus et al. (2018) (left panel) to the $\lambda = 1.6\,\mu$m polarized intensity image from our $2M_{\rm J}$ simulation (right panel). Our model replicates the upper and lower disk surface shape, extending out to the same approximate radius. Most interesting is that we reproduce the inner spirals in the SPHERE data. In our model these are caused by the propagation of the planet wake in the upper layers of the disk. The simulated spirals from the planet extend to the edge of the emitting surface, as in the observations. The dark line along the upper left diagonal from the center of the model image is caused by the phase function of the polarization

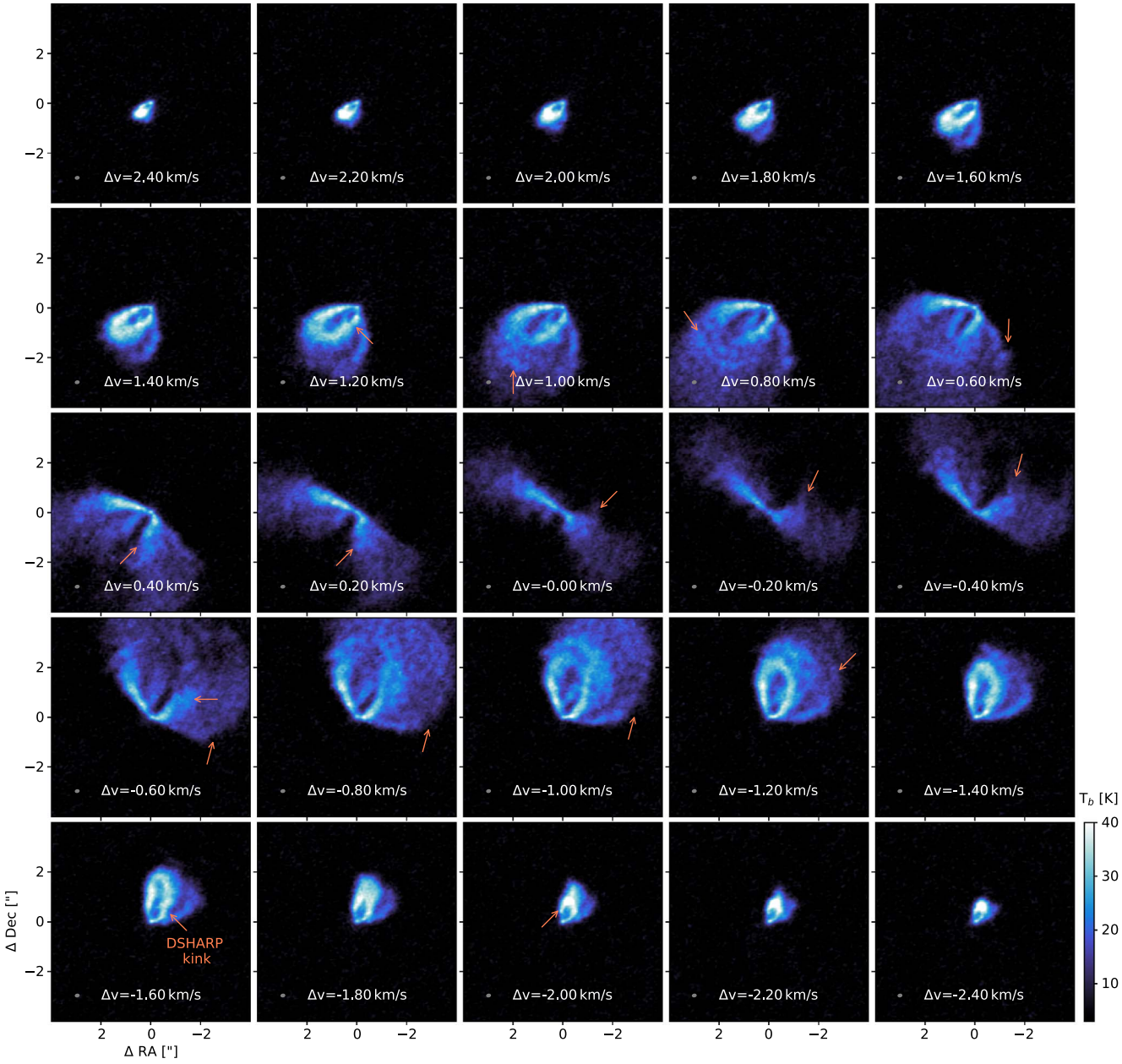

Figure 1. Channel maps of ^{12}CO $J = 2$–1 line emission in IM Lupi (Oberg et al. 2021). Arrows identify non-Keplerian velocity perturbations visible in the data, including the tentative kink identified in the DSHARP data by Pinte et al. (2020) (lower left panel). The channel maps for IM Lupi are available at the MAPS website: https://alma-maps.info/data.html.

(Pinte et al. 2006). A drop in polarized intensity is also visible along the same diagonal in the observations.

3.3. Tracing the Planet Wake in the Outer Disk

A key prediction from our model is that the planetary wake should produce coherent velocity perturbations tracing the wake in the outer disk. That is, the non-Keplerian features seen in Figure 1 should trace the specific morphology of a planet wake, as opposed to being a series of flocculent spiral arms from gravitational instability. Calcino et al. (2022) found that the planet wake in the HD 163296 disk was best traced in the peak velocity map.

Figure 4 compares the observed peak velocity map computed from the CO cube for IM Lupi supplied by the MAPS team (Law et al. 2021; left) to the same predicted from our $2M_J$ model (right). To make the comparison clear, we overlaid both plots with a dotted line showing the analytic spiral wake (Rafikov 2002) best matching our simulation model, projected to the upper disk surface using the ^{12}CO-emitting surface height calculated by Law et al. (2021; following Pinte et al. 2018a). In both the model and the observations, we observe velocity perturbations that trace the planet wake through the outer disk. The distorted contours in the observational data appear to follow the planet wake both inside and outside the planet location, particularly in the second spiral. Particularly intriguing is the "N-wave" structure apparent in the distorted contours around the dashed line in the observational map, which are predicted by both our simulations (right panel) and by semianalytic models of planet wake propagation (Rafikov 2002; Bollati et al. 2021).

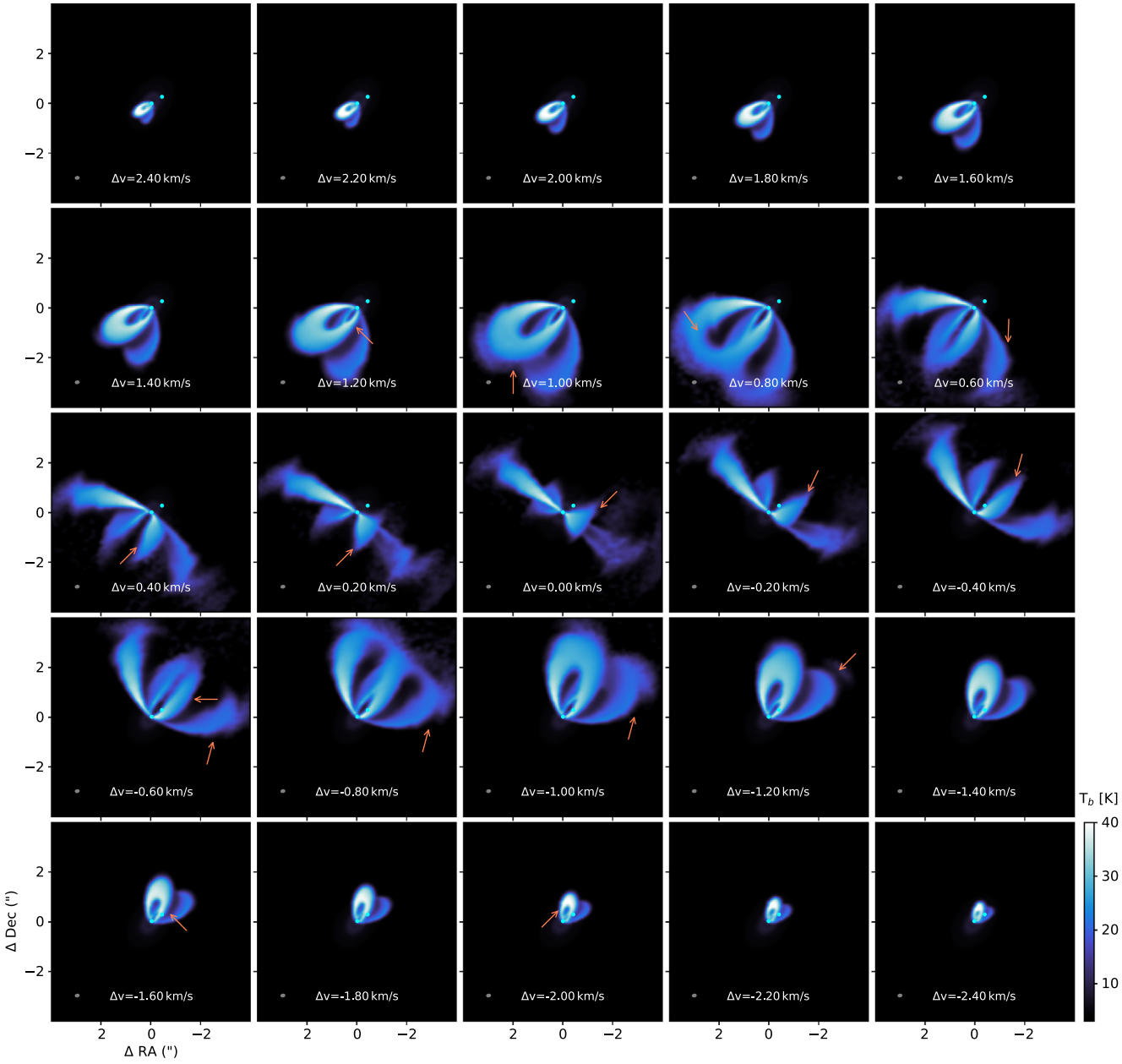

Figure 2. As in Figure 1, but showing synthetic ^{12}CO $J = 2$–1 line emission from our 3 $M_{\rm Jup}$ simulation, postprocessed with MCFOST and convolved with the observational beam. All of the non-Keplerian features labeled with arrows in Figure 1 find counterparts in our model, caused by the planet wake propagating through the disk. Our synthetic data cube of the IM Lupi protoplanetary disk is available on FigShare: doi:10.26180/20145620.v3.

Patches of red and blue seen in the bottom right of the data are simply where the lower surface of the disk becomes visible in the peak velocity map; this is reproduced in our model.

3.4. Continuum Emission and Planet Mass Estimate

Figure 5 shows the continuum emission (left column) and selected CO channels (right columns) from each of the four simulations to data from DSHARP and MAPS (Andrews et al. 2018; Czekala et al. 2021; top row).

The kink observed by Pinte et al. (2020) is located in the $\Delta v = -1.60\,{\rm km\,s^{-1}}$ channel, which is also seen in our simulations. Some additional perturbations (or "secondary kinks") can be seen on both the upper and lower surfaces, as in Figure 1. These correspond to velocity perturbations created by the planet wake.

Comparing the DSHARP continuum (Andrews et al. 2018; top panels) to the four simulations (bottom four panels), on all simulation models we observe an $m = 2$ spiral in the disk, increasing in amplitude with planet mass. For larger planet masses the simulations also show the formation of a gap in the outer ring, carved by the planet. However for planet masses $\geqslant 5\,M_{\rm Jup}$ the amplitude of the scattered-light spirals are too high compared to the data (Figure 3), so we favor a planet mass of 2–3 $M_{\rm Jup}$.

4. Discussion

In this Letter we explored whether an embedded planet can explain the spiral arms, non-Keplerian motions, and scattered-light emission in the IM Lupi disk. With caveats, we find that a single planet of several times the mass of Jupiter orbiting at

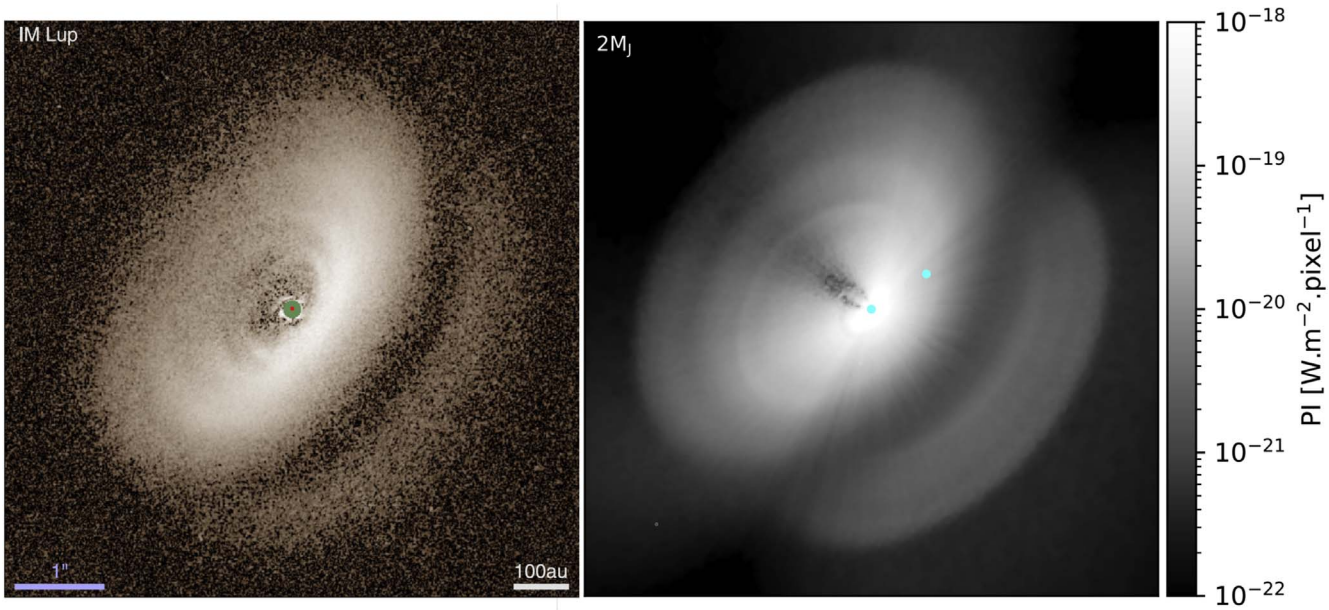

Figure 3. Scattered light. Left: VLT/SPHERE image from Avenhaus et al. (2018) using differential polarimetric imaging. Right: synthetic polarized intensity image at 1.6 μm from our 2M_J simulation. Panels are 6.″4 × 6.″4. Cyan dots show positions of the star and planet, respectively. The planet wake in our model reproduces the spiral substructure observed in the upper layers of the disk. A FITS file of our radiative transfer image is available on FigShare: doi:10.26180/20145620.v3.

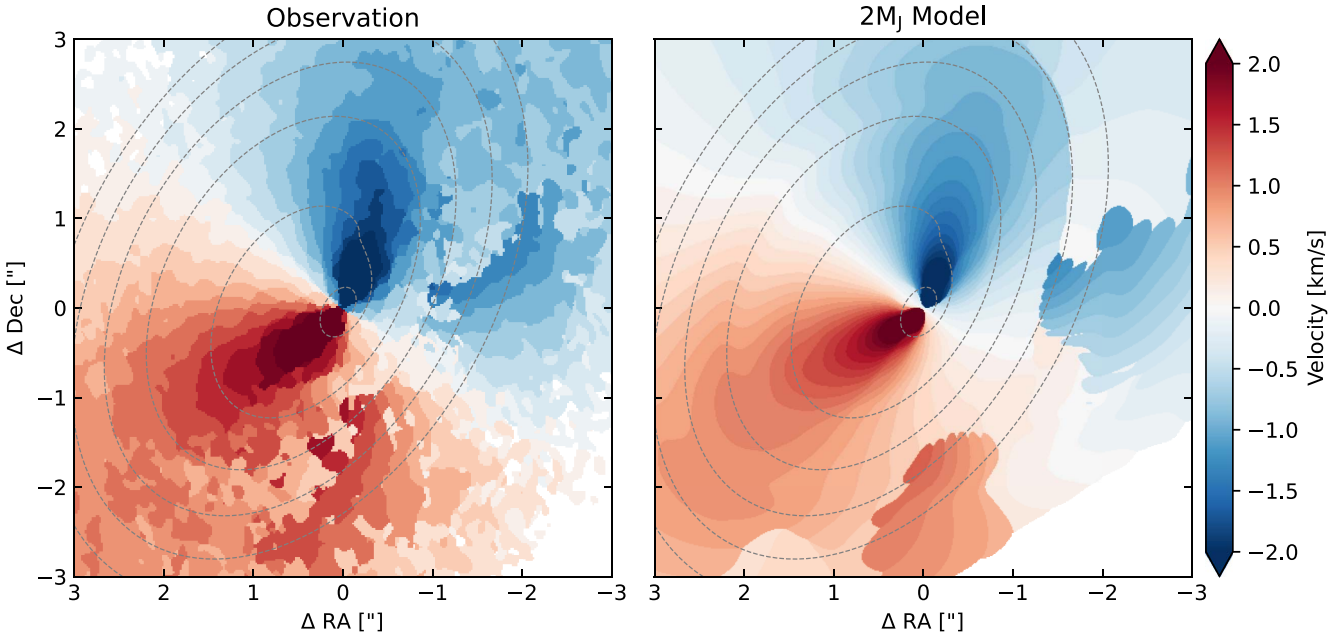

Figure 4. Left panel: peak velocity map in ^{12}CO emission from MAPS (Oberg et al. 2021) data. Right panel: synthetic map from our 2M_J model. The simulated 2M_J result uses $\Delta v = 0.2$ km s^{-1}. Dotted line (overlaid on both our simulation model and the observations) shows the expected location of the spiral wake, projected to the upper ^{12}CO-emitting surface layer height derived by Law et al. (2021).

≈100–120 au can simultaneously explain all of these features. Our best evidence for a planet is in the kinematics. We confirm that the tentative kink is found by Pinte et al. (2020) in the new data from MAPS (Oberg et al. 2021). However, this is not the only kink in the data. In particular, a series of "secondary kinks" (Bollati et al. 2021) appear to trace the planet wake in the observations in a manner predicted by our simulations. These are best seen in the observed peak velocity map (Figure 4), as recently demonstrated for the planet in the HD 163296 disk (Pinte et al. 2018b; Calcino et al. 2022).

To reproduce the disk morphology in scattered light (with or without a planet) we needed the grains responsible for scattered-light emission to be well coupled to the gas, and for the disk to be optically thick at 1.6 μm. In our hydrodynamic model we simulated a range of grain "sizes"—assuming spherical grains and an intrinsic grain density of 3 g cm^{-3}—from 1 μm to 2.3 mm, corresponding to Stokes numbers of 10^{-4} and 0.2 at 100 au, respectively (e.g., using Equation (3) in Dipierro et al. 2015). In the radiative transfer calculation we needed an additional factor of 10 scaling (down) in the Stokes number to avoid settling of the grains responsible for the scattered-light emission out of the disk atmosphere. This is not surprising as Cleeves et al. (2016) already inferred that micron-sized grains have the same scale height as the gas in IM

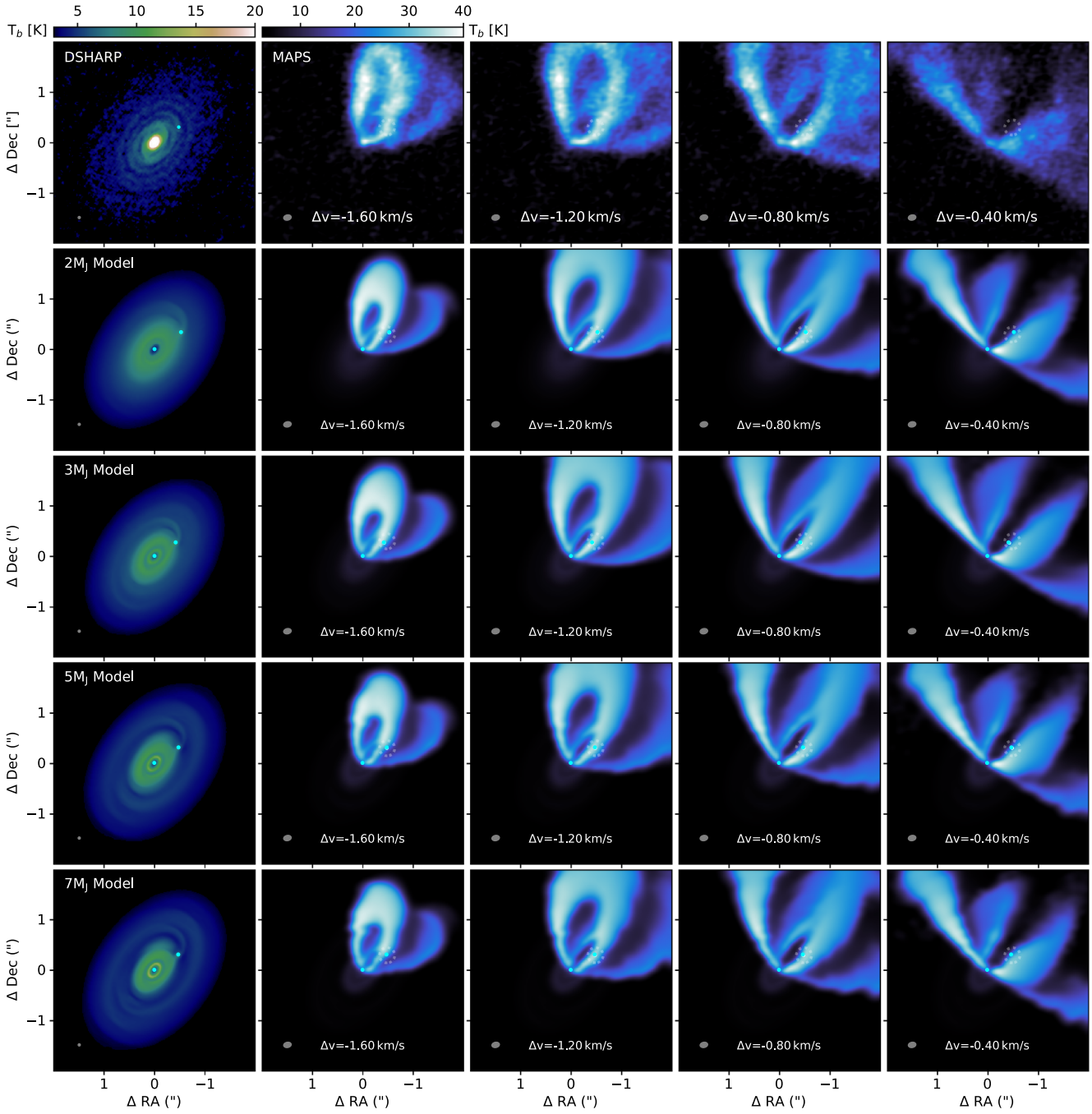

Figure 5. Effect of planet mass, comparing simulations (bottom rows) with observed dust continuum emission (left column) and selected ^{12}CO channels (right columns). Blue dot shows the expected planet position, while the gray circle indicates predicted location of the planet at 117 au (Pinte et al. 2020). Filled ellipse gives beam size. Radiative transfer images and cubes are available on FigShare: doi:10.26180/20145620.v3.

Lupi ($h = 12$ au at $r = 100$ au) and that the scale height of millimeter-emitting grains is $\approx 4\times$ smaller. This likely indicates that grains are fluffy aggregates rather than compact spheres, as already suggested for IM Lupi by Pinte et al. (2008) and by ALMA polarization observations (Hull et al. 2018).

Elias 2–27 is the other main disk that shows $m = 2$ spiral arms in continuum emission (Huang et al. 2018). The hypotheses are a planet, or gravitational instability (Meru et al. 2017; Forgan et al. 2018). Gravitational instability can lead to formation of multiple spiral arms and possibly fragmentation to form gas giants (Kimura & Tsuribe 2012; Kratter & Lodato 2016) and hence may also explain the main phenomena seen in IM Lupi. But one would need to posit that the inner disk is unstable (to produce spiral arms) while the outer disk, being relatively featureless in continuum, is not. This is opposite to the expected scenario where the outer disk is more unstable (Kratter & Lodato 2016). The global condition for instability is $M_{\rm disk}/M_* \gtrsim H/R$ (Toomre 1964). With $M_{\rm disk} = 0.1\ M_\odot$ the disk-to-star mass ratio is $0.1/1.12 = 0.09$, which is smaller than the inferred $H/R \approx 0.12$ at 100 au, and hence suggests that the disk is stable. Sierra et al. (2021) estimated a Toomre $Q \approx 2$ at $r \gtrsim 50$ au in IM Lupi, suggesting the disk is gravitationally stable. We neglected self-gravity in our models, but the above discussion suggests that it could be

important in IM Lupi, even if not ultimately responsible for the spiral arms.

Planets in protoplanetary disks migrate (Ward 1986). In PHANTOM, sink particles are free to interact with gas and dust, and hence migrate. We found that the $5M_J$ planet migrated at ≈ 2 au kyr^{-1} after gap opening. Additionally, the migration depends on the planet mass, with more massive planets migrating faster. This can be seen in Figure 5 by comparing the gray circles (indicating the 117 au estimate) and the simulated location. Migration—which can be inward or outward depending on disk properties—makes it difficult to predict the radial location of the planet and brings a coincidence problem as to why any planet would be observed at a particular location. Nevertheless, we have shown that a planet in the right location can explain all the main substructures observed in IM Lupi.

5. Conclusions

1. A single embedded 2–3 $M_{\rm Jup}$ planet orbiting at ≈ 110 au in the IM Lupi circumstellar disk can simultaneously explain the 16 different localized deviations from Keplerian motion ("kinks") seen in the ^{12}CO channel maps.
2. The same planet can explain the spiral arms seen in the upper layers of the disk in scattered light and the $m = 2$ spiral arms seen in continuum emission.
3. We predict, and confirm, that the wake from the planet should be visible in the observational peak velocity map from the ^{12}CO emission line. The perturbations seen in this map (Figure 4, left panel) closely match the prediction for the planet-generated spiral arm

We required a relatively massive disk ($\approx 0.1\,M_\odot$) as well as a scaled Stokes number for the dust grains to remain well coupled in both the upper layers and midplane of the disk. Such a disk mass suggests that gravitational instability may also be possible (but with Sierra et al. 2021 finding $Q_{\rm min} \sim 2$).

D.J.P. thanks Judit Szulagyi for useful discussions about the perils of vacuum cleaner sink particles at the "Kinematics of Planet Formation" meeting in 2019; also Giuseppe Lodato and Richard Teague for useful discussions. J.C. acknowledges support from LANL/LDRD program (approved for release as LA-UR-21-31387). We used OzSTAR and Gadi supercomputing facilities funded by Swinburne University (OzSTAR) and the Australian Government via the National Computing Initiative. D.P. and C.P. acknowledge Australian Research Council funding via DP180104235 and FT170100040. We made use of ALMA data: ADS/JAO.ALMA#2018.1.01055.L, ADS/JAO.ALMA#2016.1.00484.L. ALMA is a partnership of ESO (representing its member states), NSF (USA) and NINS (Japan), together with NRC (Canada), MOST and ASIAA (Taiwan), and KASI (Republic of Korea), in cooperation with the Republic of Chile. We thank the referee for useful suggestions.

Appendix
Residuals from Keplerian Rotation

To assess the significance of the non-Keplerian features in the channel maps presented in Figures 1 and 2, Figure 6 shows the absolute brightness temperature residuals in the channel maps when the model with no planet is subtracted from the model shown in Figure 2. Arrows reproduced from Figures 1– and 2 all point to correspondingly significant features ($\Delta T_b > 10$ K; corresponding to a signal-to-noise ratio of $\gtrsim 7$) in the residual maps. We found similar results when subtracting an azimuthally averaged model.

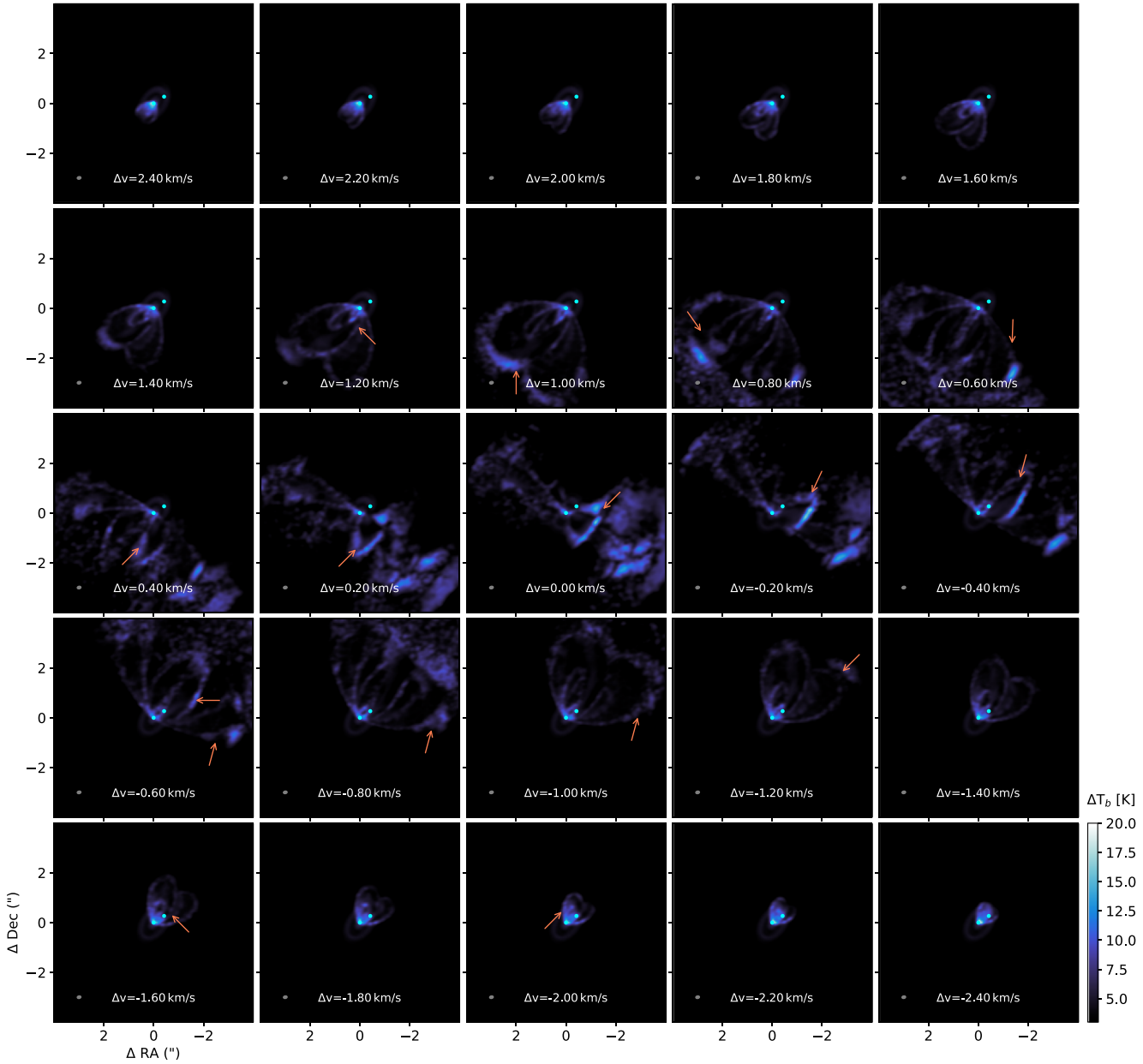

Figure 6. Absolute brightness temperature residuals in channel maps of ^{12}CO $J = 2$–1 line emission after subtracting a model with no planet from the model shown in Figure 2, highlighting significant non-Keplerian features in individual channels caused by the embedded planet. Arrows are as identified from observations in Figure 1.

ORCID iDs

Harrison J. Verrios https://orcid.org/0000-0003-3803-3855
Daniel J. Price https://orcid.org/0000-0002-4716-4235
Christophe Pinte https://orcid.org/0000-0001-5907-5179
Thomas Hilder https://orcid.org/0000-0001-7641-5235
Josh Calcino https://orcid.org/0000-0001-7764-3627

References

Andrews, S., Huang, J., Perez, L. M., et al. 2018, ApJL, 869, L41
Avenhaus, H., Quanz, S. P., Garufi, A., et al. 2018, ApJ, 863, 44
Ayliffe, B. A., & Bate, M. R. 2010, MNRAS, 408, 876
Ballabio, G., Dipierro, G., Veronesi, B., et al. 2018, MNRAS, 477, 2766
Bollati, F., Lodato, G., Price, D. J., & Pinte, C. 2021, MNRAS, 504, 5444
Calcino, J., Hilder, T., Price, D. J., et al. 2022, ApJL, 929, L25
Cleeves, L. I., Öberg, K. I., Wilner, D. J., et al. 2016, ApJ, 832, 110
Czekala, I., Loomis, R. A., Teague, R., et al. 2021, ApJS, 257, 2
Dipierro, G., Price, D., Laibe, G., et al. 2015, MNRAS, 453, L73
Forgan, D. H., Ilee, J. D., & Meru, F. 2018, ApJL, 860, L5
Hall, C., Dong, R., Teague, R., et al. 2020, ApJ, 904, 148
Hall, C., Rice, K., Dipierro, G., et al. 2018, MNRAS, 477, 1004
Huang, J., Andrews, S. M., Dullemond, C. P., et al. 2018, ApJL, 869, L42
Huang, J., Andrews, S. M., Pérez, L. M., et al. 2018, ApJL, 869, L43
Hull, C. L. H., Yang, H., Li, Z.-Y., et al. 2018, ApJ, 860, 82
Hutchison, M., Price, D. J., & Laibe, G. 2018, MNRAS, 476, 2186
Kimura, S. S., & Tsuribe, T. 2012, PASJ, 64, 116
l Lindegren, L., Hernández, J., Bombrun, A., et al. 2018, A&A, 616, A2
Kratter, K., & Lodato, G. 2016, ARA&A, 54, 271
Law, C. J., Teague, R., Loomis, R. A., et al. 2021, ApJS, 257, 4
Meru, F., Juhász, A., Ilee, J. D., et al. 2017, ApJL, 839, L24
Oberg, K. I., Guzman, V. V., Walsh, C., et al. 2021, ApJS, 257, 1
Paneque-Carreño, T., Pérez, L. M., Benisty, M., et al. 2021, ApJ, 914, 88
Panić, O., Hogerheijde, M. R., Wilner, D., & Qi, C. 2009, A&A, 501, 269
Pinte, C., Harries, T. J., Min, M., et al. 2009, A&A, 498, 967
Pinte, C., Ménard, F., Duchêne, G., et al. 2018a, A&A, 609, A47
Pinte, C., Ménard, F., Duchêne, G., & Bastien, P. 2006, A&A, 459, 797
Pinte, C., Padgett, D. L., Ménard, F., et al. 2008, A&A, 489, 633

Pinte, C., Price, D. J., Ménard, F., et al. 2018b, ApJL, 860, L13
Pinte, C., Price, D. J., Ménard, F., et al. 2020, ApJL, 890, L9
Pinte, C., van der Plas, G., Ménard, F., et al. 2019, NatAs, 3, 1109
Price, D. J., & Laibe, G. 2015, MNRAS, 451, 813
Price, D. J., & Monaghan, J. J. 2007, MNRAS, 374, 1347
Price, D. J., Wurster, J., Tricco, T. S., et al. 2018, PASA, 35, e031
Rafikov, R. R. 2002, ApJ, 569, 997
Sierra, A., Pérez, L. M., Zhang, K., et al. 2021, ApJS, 257, 14
Szulágyi, J., Masset, F., Lega, E., et al. 2016, MNRAS, 460, 2853
Toomre, A. 1964, ApJ, 139, 1217
Veronesi, B., Paneque-Carreño, T., Lodato, G., et al. 2021, ApJL, 914, L27
Ward, W. R. 1986, Icar, 67, 164
Weingartner, J. C., & Draine, B. T. 2001, ApJ, 548, 296